

Selective Laser Melting of 316L Stainless Steel: Physics of Melting Mode Transition and Its Influence on Microstructural and Mechanical Behavior

AKASH AGGARWAL,¹ SUSHIL PATEL,¹ and ARVIND KUMAR^{1,2}

1.—Department of Mechanical Engineering, Indian Institute of Technology Kanpur, Kanpur 208016, India. 2.—e-mail: arvindkr@iitk.ac.in

A combined computational–experimental study is performed to investigate the effect of melting modes (conduction, transition and keyhole) on 316L stainless steel parts fabricated by selective laser melting. A high-fidelity mesoscale model is developed using the LIGGGHTS and OpenFOAM open-source codes to describe the physical phenomena (convection, melting, evaporation and solidification), melt flow dynamics and melting mode transition. The developed model helps to understand laser/matter interaction, melting of particles, the effect of recoil pressure and the formation of fusion zone. The computational results were found consistent with the single-track experimental results. Furthermore, for establishing the influence of melting mode on microstructural and mechanical properties, bulk samples with different melting modes were fabricated and characterized by comparing the microstructure, microhardness, nanohardness and tensile behavior. The experimental results showed that the stable keyhole mode results in higher hardness, higher elongation and finer cellular grains compared with the conduction mode.

INTRODUCTION

Selective laser melting (SLM), the most popular metal additive manufacturing (AM) process, is well suited for making complicated parts that are difficult to manufacture by conventional manufacturing techniques. Currently, the main bottlenecks inhibiting the usage of the SLM parts include problems such as the low resolution, low surface finish quality and low build rate.¹ To overcome the aforesaid problems, the latest SLM machines are now being equipped with a laser with a small spot radius for an enhanced resolution and surface finish and high power to increase the build rate.² The combination of high power and a small spot radius leads to high energy density, exceeding the threshold value, resulting in the transition of the melting mode in the SLM process from conduction to keyhole mode. The energy density in the conduction mode of melting is only high enough to melt the metal, and the maximum temperature achieved is below the vaporization temperature.³ Melting is achieved by the conduction of the laser heat flux from the

surface, resulting in melt pools that are shallow and wider. However, in the keyhole mode of melting, due to extremely high energy density, metal vaporizes and plasma is formed. The formation of a vapor cavity substantially increases the beam absorption enabling the laser to penetrate deeper, resulting in melt pools that are deeper and narrower.^{4–6} The conduction mode leads to high-quality stable melt pool formation with reduced spatter generation, whereas the keyhole mode of melting results in high penetration melts leading to enhanced productivity. Some works have reported about the melting mode transition with increasing power during the SLM process,^{2,7–10} but its influence on the melting dynamics, microstructural and mechanical behavior is not understood mathematically or experimentally.

In this article, a high-fidelity mesoscale model is developed using the LIGGGHTS and OpenFOAM open-source codes to study the melting mode transition, attendant physical phenomena (convection, melting, evaporation and solidification) and melt flow dynamics occurring in the SLM process. The

discrete element method is used to determine the spatial arrangement of the particles in the powder layer. Thereafter, the volume of fluid approach using the finite volume method is used to identify and track the interface of the powder particles undergoing phase transition. Subsequently, geometrical characteristics of the melt pool under different melting modes (conduction, transition and keyhole) obtained by computational modeling are validated with the in-house single-track experiments. Finally, the microstructure and mechanical properties of the bulk samples fabricated with different melting modes are investigated and compared.

MELTING MODE TRANSITION

The melting mode is changed by defocusing, keeping all other process parameters the same. In SLM, defocusing is achieved by the upward or downward movement of the substrate plate with reference to the focal position of the laser beam. As shown in Fig. 1a, depending on the shift direction, defocusing can be either positive or negative. For negative defocusing, the substrate is positioned above the focal plane of the laser beam, while for positive defocusing, the substrate is positioned below the focal plane.¹¹ The amount of defocusing is controlled by the defocus distance (f_d), which in turn modifies the energy density because of spot size change.

The relationship of the spot radius (R_{spot}) and defocus distance (f_d) is given by¹²

$$R_{\text{spot}} = R_0 \sqrt{1 + \left(\frac{f_d}{f_R}\right)^2} \quad (1)$$

where R_0 is the spot radius at the focal plane, and f_R denotes the Rayleigh length. The Rayleigh length (f_R) is given by

$$f_R = \frac{\pi R_0^2}{\lambda} \quad (2)$$

where λ denotes the wavelength of the Gaussian beam. The Rayleigh length specifies the distance along the beam travel direction from the waist to the location where the cross-sectional area is doubled. In the current study, experiments were performed using the Concept Laser MLabR machine, which is equipped with a 100-W continuous wave-modulated ytterbium fiber laser with a wavelength of 1070 nm and focused beam diameter of 50 μm resulting in a Rayleigh length (f_R) of 1.835 mm.

The volumetric energy density (E_d) considering the spot radius is given by¹³

$$E_d = \frac{P}{2vR_{\text{spot}}t_p} \quad (3)$$

where P is the laser power, v is the beam traversal velocity, and t_p is the powder layer thickness. In this study, the laser power (P), scanning speed (v) and

thickness of the powder layer (t_p) were optimized to 100 W, 700 mm/s and 25 μm , respectively. Different positive defocus distances (f_d) of 0 mm ($R_{\text{spot}} = 25 \mu\text{m}$, $E_d = 114.28 \text{ J mm}^{-3}$), 1.5 mm ($R_{\text{spot}} = 32.29 \mu\text{m}$, $E_d = 88.48 \text{ J mm}^{-3}$) and 3 mm ($R_{\text{spot}} = 47.90 \mu\text{m}$, $E_d = 59.65 \text{ J mm}^{-3}$) were chosen in this study to change the melting mode to keyhole, transition and conduction, respectively.

NUMERICAL MODELING AND METHODOLOGY

To understand the interaction of the high energy beam with the powder layer and the resulting melting mode transition, single track scanning over a powder layer is simulated with the help of a thermo-fluidic powder scale model developed using an integrated discrete element method (DEM)-computational fluid dynamics (CFD) approach. The developed thermo-fluidic powder scale model uses a realistic powder bed for CFD modeling and incorporates the physics of laser irradiation on the powder bed, melt flow due to thermo-capillary force, effect of the recoil pressure and the phase transition (melting, solidification, evaporation and condensation).

Single Layer Powder Bed Generation

Spatial information of the powder particles (size and location) in the powder layer laid over the substrate is critical for mesoscale modeling, but it is challenging to determine it experimentally.¹⁴ Therefore, alternative strategies, such as computational modeling, become effective tools to obtain precise information on the size and location of the powder particles. The present work uses a DEM-based modeling approach to simulate the powder spreading process. DEM, a Lagrangian-based approach, calculates forces acting on granular material from the initial conditions, governing physical laws and contact models. The computational domain considers each particle as an individual entity with its own properties interacting with other particles and boundaries in its vicinity. The motion of each particle is described using Newton's law of motion for conservation of momentum. In this work, a LIGGGHTS (LAMMPS Improved for General Granular and Granular Heat Transfer Simulations) open-source DEM code¹⁵ is used for powder spreading. First, the particle size distribution (PSD) is experimentally measured by performing image analysis on the SEM (scanning electron microscopy) micrographs. Then, a cloud of randomly generated particles with the experimentally measured PSD is generated inside the DEM computational domain and allowed to fall under gravity; after all the powder particles have settled, a recoater deposits a 25- μm -thick layer.^{16,17} Thereafter, using a MATLAB script, the particle information is exported to an OpenFOAM (Open Field Operation

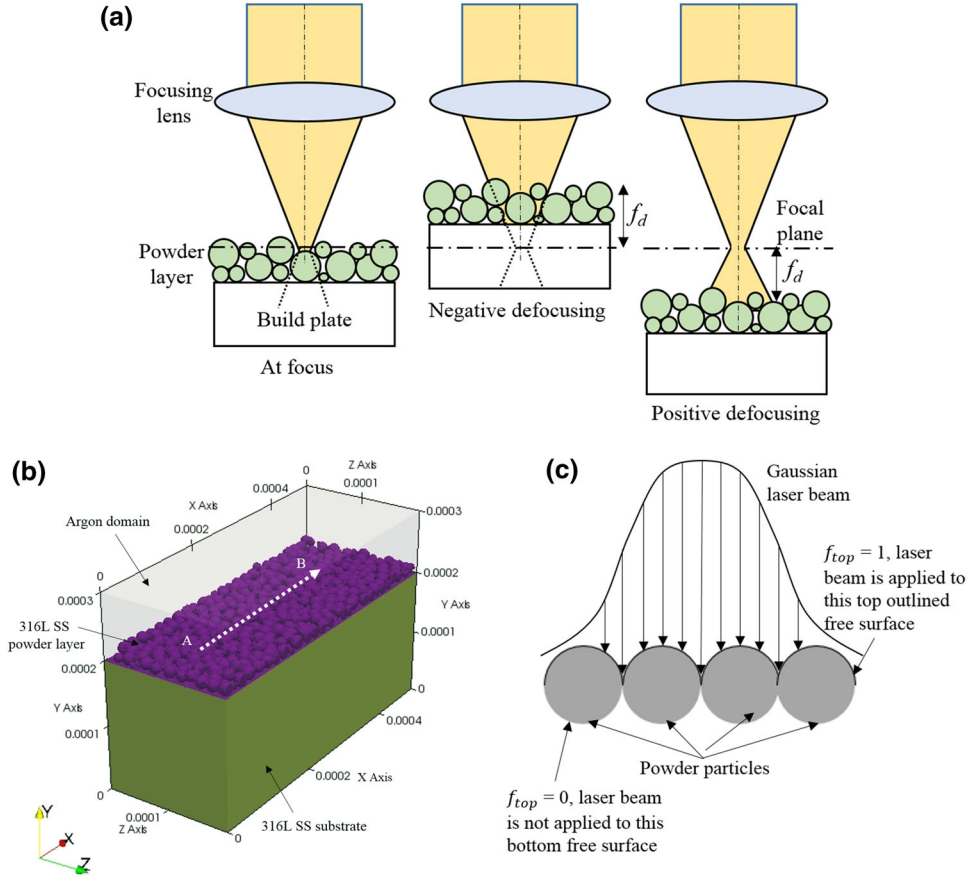


Fig. 1. (a) Schematic showing the powder bed position at focus, negative defocus and positive defocus, respectively. (b) Computational domain used for CFD simulation (labels in X , Y , Z axis are distance in m). (c) Absorption of the Gaussian beam by the powder particles.

and Manipulation) open-source CFD C++ code.¹⁸ The CFD model of thermo-fluidic phenomena, presented in the following, is developed in OpenFOAM.

Free Surface Thermo-Fluidic Modeling

Figure 1b shows the computational domain considered for the single-track thermo-fluidic simulation. The computational domain consists of a 316L stainless steel substrate ($500 \times 200 \times 200 \mu\text{m}^3$), an argon inert gas region ($500 \times 100 \times 200 \mu\text{m}^3$) and a $25\text{-}\mu\text{m}$ -thick 316L stainless steel powder layer. The laser beam traverses a distance of $350 \mu\text{m}$ from point A to point B. In the model, transient heat transfer and fluid flow dynamics in the melt pool are considered using the volume of fluid surface tracking method (VOF). The VOF method captures the interface between the metal (powder particles, substrate) and the inert gas.

The VOF transport equation for interface tracking between two immiscible phases (316L stainless steel and argon gas) is given by¹⁹

$$\frac{\partial \gamma}{\partial t} + \nabla \cdot (\gamma \vec{U}) + \nabla \cdot ((1 - \gamma) \gamma \vec{U}_r) = 0 \quad (4)$$

where γ is the phase fraction, \vec{U} is the velocity vector, and \vec{U}_r is the compression velocity. The compression velocity compresses the interface by minimizing the numerical diffusion of the phase fraction γ while maintaining its boundedness.

The phase fraction γ in Eq. 4 denotes the ratio of the volume occupied by the metallic phase (V_{metal}) to the total volume of the cell (V) and is given by

$$\gamma(\vec{x}, t) = \frac{V_{\text{metal}}}{V} = \begin{cases} 1 & \vec{x} \in \text{metal (solid and liquid)} \\ 0 < \gamma < 1 & \vec{x} \in \text{interface} \\ 0 & \vec{x} \in \text{inert gas} \end{cases} \quad (5)$$

In the simulation, the thermo-physical properties of the two immiscible phases are calculated using the continuum formulation based on the classical mixture theory. The volume-fraction average of a general thermo-physical property x is given as

$$x = \gamma x_{\text{metal}} + (1 - \gamma) x_{\text{gas}}, \quad x \in [\rho, \mu, C_p, k] \quad (6)$$

where the symbols ρ , μ , C_p and k represent the density, dynamic viscosity, specific heat and

thermal conductivity, respectively. The term x_{metal} in Eq. 6 represents the thermo-physical properties of the metallic phase and is given by

$$x_{\text{metal}} = x_{\text{liquid,metal}} f_{\text{liquid,metal}} + x_{\text{solid,metal}} (1 - f_{\text{liquid,metal}}) \quad (7)$$

where $f_{\text{liquid,metal}}$ is the liquid fraction in the metallic phase. Assuming the flow to be incompressible, laminar and Newtonian, the governing conservation equations for mass, momentum and energy conservation are formulated.

The governing energy conservation equation is given by

$$\frac{\partial(\rho C_p T)}{\partial t} + \nabla \cdot (\rho \vec{U} C_p T) = \nabla \cdot (k \nabla T) + S_{\text{Latent}} + Q_{\text{Losses}} + Q_{\text{Laser}} \quad (8)$$

The source term S_{Latent} in Eq. 8 accounts for the evolution of the latent heat during phase change. This term is given by

$$S_{\text{Latent}} = \begin{cases} -L \frac{\partial}{\partial t} (\rho f_{\text{liquid,metal}}) & \text{for } \gamma = 1 \\ 0 & \text{for } \gamma < 1 \end{cases} \quad (9)$$

In (Eq. 9), L is the latent heat of fusion. The liquid fraction of the metallic phase is determined by the enthalpy-porosity approach.²⁰

The source term Q_{Losses} in Eq. 8 represents evaporation heat loss, radiation heat loss and convective heat loss due to the flowing argon gas. It is defined as

$$Q_{\text{Losses}} = (q''_{\text{evaporation}} + q''_{\text{radiation}} + q''_{\text{convection}}) |\nabla \gamma| \frac{2\rho C_p \text{eff}}{\rho_{\text{metal}} C_p \text{metal} + \rho_{\text{gas}} C_p \text{gas}} \quad (10)$$

As the temperature exceeds the boiling point, the evaporative heat loss needs to be considered. The evaporative heat loss is the product of the latent heat of vaporization L_v and the vaporized mass flow rate \dot{m}_v .

$$q''_{\text{evaporation}} = -L_v \dot{m}_v \quad (11)$$

The vaporized mass flow rate of the escaping vapor \dot{m}_v is given by:

$$\dot{m}_v = (1 - \beta) \frac{MP_v}{\sqrt{2\pi MRT}} \quad (12)$$

where M is the molar mass, R is the ideal gas constant, and P_v is the recoil vapor pressure, which is given by²¹

$$P_v = 0.54 P_0 \exp \left[\frac{L_v M (T - T_v)}{RT T_v} \right] \quad (13)$$

where P_0 is the atmospheric pressure, L_v is the latent heat of vaporization, and T_v is the vaporization temperature.

β in Eq. 12 is the retro-diffusion coefficient and represents the extent of condensation of escaping vapor. In this study, $\beta = 0.18$ is assumed.¹⁷

The heat flux losses due to radiation and convection are given by:

$$q''_{\text{radiation}} = -\sigma_b \varepsilon (T^4 - T_\infty^4) \quad (14)$$

$$q''_{\text{convection}} = -h(T - T_\infty) \quad (15)$$

where ε is the emissivity, σ_b is the Stefan-Boltzmann constant, h is the convective heat transfer coefficient, and T_∞ is the ambient temperature.

The source term Q_{Laser} in Eq. 8 accounts for heating by the moving laser beam. The energy input from the laser beam is approximated by a Gaussian distribution and is defined as

$$Q_{\text{Laser}} = \frac{2\eta P}{\pi R_{\text{spot}}^2} \exp \left[-2 \frac{(x - x_i - vt)^2 + (z - z_i)^2}{R_{\text{spot}}^2} \right] f_{\text{top}} |\nabla \gamma| \frac{2\rho C_p \text{eff}}{\rho_{\text{metal}} C_p \text{metal} + \rho_{\text{gas}} C_p \text{gas}} \quad (16)$$

where η is the absorption coefficient, v is the laser traversal velocity, (x_i, z_i) denotes the beginning point of the laser melting, and f_{top} , as shown in Fig. 1c, is the unit function representing the top portion of the powder particle where heat flux is applied.

The mass conservation equation for incompressible flow is given by

$$\nabla \cdot (\vec{U}) = 0 \quad (17)$$

The momentum conservation equation is given by

$$\begin{aligned} \frac{\partial(\rho \vec{U})}{\partial t} + \vec{U} \cdot \nabla(\rho \vec{U}) = & -\nabla p + \nabla \cdot \left(\mu \left(\nabla \vec{U} + (\nabla \vec{U})^T \right) \right) + \vec{F}_N \\ & + \vec{F}_D + \vec{F}_S \end{aligned} \quad (18)$$

The buoyant force due to the natural convection is implemented in the current model with the help of a source term \vec{F}_N in Eq. 18, which is given as

$$\vec{F}_N = \rho_l g \beta_T (T - T_{\text{ref}}) \quad (19)$$

where ρ_l , β_T and T_{ref} are the liquid metal density, thermal expansion coefficient and reference temperature, respectively.

The source term \vec{F}_D appearing in Eq. 18 is defined in Eq. 20. It aids to smoothly bring down the velocity of the fluid at the liquid–solid interface and makes the fluid velocity in the un-melted solid zone zero.

$$\vec{F}_D = \frac{(1 - f_{\text{liquid,metal}})^2}{f_{\text{liquid,metal}}^3 + b} C \vec{U} \quad (20)$$

The constant C in Eq. 20 represents the mushy zone constant, and a value of $160,000 \text{ kg m}^{-3} \text{ s}^{-1}$ is considered in the current model.²² The term b is another constant having a small value ($\sim 10^{-6}$) and is used to prevent division by zero when the liquid fraction ($f_{\text{liquid,metal}}$) becomes zero. The source term \vec{F}_S in Eq. 18 represents the forces that are acting at the interface and is given by

$$\vec{F}_S = \left\{ \sigma \kappa \hat{n} + \frac{d\sigma}{dT} [\nabla T - \hat{n}(\hat{n} \cdot \nabla T)] + \hat{n}(P_v) \right\} |\nabla \gamma| \frac{2\rho}{\rho_m + \rho_g}$$

where σ is the surface tension coefficient, $\kappa = -(\nabla \cdot \hat{n})$ is the mean curvature of the free surface, $\hat{n} = \nabla \gamma / |\nabla \gamma|$ is the interface normal unit vector, and $d\sigma/dT$ is the temperature coefficient of surface tension. The first term is the surface tension force acting normally to the interface, the second term is the force due to Marangoni convection acting tangentially at the interface, and the third term is the recoil pressure exerted by the metal vapor on the top surface of the molten pool. The term $2\rho/(\rho_m + \rho_g)$ redistributes the smeared forces toward the denser phase (316L stainless steel) so that spurious currents in the gas phase can be avoided.

Numerical Details

For thermo-fluidic CFD simulation, an element size of $2.5 \mu\text{m}$ provides mesh independent and computationally efficient results; hence, simulations are performed using this mesh. The total number of Cartesian mesh elements used in the CFD simulation is 1.92 million, and the physical time is $500 \mu\text{s}$. To make sure the solution is stable, the self-adaptive time step based on the Courant-Friedrichs-Lewy (CFL) condition is used. For each time step, volume fraction advection, continuity, momentum and energy transport equations are solved. The VOF equation in OpenFOAM is iteratively solved using the multi-dimensional universal limiter with the explicit solution (MULES) method. The high-fidelity CFD simulations of the single-track traversal are performed using 40 cores on a high-performance computing cluster, and it takes around 120 h of computational time. The material properties of 316L stainless steel used in this simulation are taken from Refs. ¹⁷ and ²³.

MATERIALS, METHODS AND EXPERIMENTS

A set of preliminary experiments was performed for 316L stainless steel powder in order to achieve a density $> 99\%$. The combination of laser power (P), scanning speed (v), hatch spacing (h) and powder layer thickness (t) of 100 W, 700 mm/s, $56 \mu\text{m}$ and $25 \mu\text{m}$, respectively, was able to fabricate nearly porosity free samples. Using these parameters, fabrication of single-track experiments and the bulk specimen was carried out to investigate the

influence of the melting mode. The melting mode transition (conduction, transition and keyhole) was observed by defocusing resulting in varying laser spot radii.

Coupon Fabrication with Single-Track Traversal

To validate the simulation results and obtain understanding of the melting mode transition, single tracks were deposited by defocusing keeping all other process parameters ($P = 100 \text{ W}$, $v = 700 \text{ mm/s}$, $t = 25 \mu\text{m}$) the same. The tracks were deposited on a $25\text{-}\mu\text{m}$ -thick 316L stainless steel powder placed on a 1-mm-thick 316L stainless steel substrate by varying the defocus distance (f_d) to 0 mm ($R_{\text{spot}} = 25 \mu\text{m}$, $E_d = 114.28 \text{ J mm}^{-3}$), 1.5 mm ($R_{\text{spot}} = 32.29 \mu\text{m}$, $E_d = 88.48 \text{ J mm}^{-3}$) and 3 mm ($R_{\text{spot}} = 47.9 \mu\text{m}$, $E_d = 59.65 \text{ J mm}^{-3}$). In total, six single-line scans of 20 mm length were made for each melting mode.

Bulk Specimen Fabrication

Three types of cuboidal samples, corresponding to each melting mode, with dimensions of $10 \times 10 \times 10 \text{ mm}^3$, were fabricated using the same set of process parameters as that of the single-track deposition using a continuous unidirectional scanning strategy with a hatch spacing of $56 \mu\text{m}$. To analyze the tensile behavior of samples in different melting modes, the tensile specimens were prepared according to the ASTM E8 M-04 standard with gauge length and diameter of 20 mm and 4 mm, respectively. For each melting mode, four specimens were fabricated.

Microstructural and Mechanical Characterization

The deposited single tracks and cuboidal specimens were cross sectioned at a center plane and then polished following standard metallographic procedures. To reveal the deposited track boundaries and solidification microstructure, the mirror polished samples were etched with $\text{H}_2\text{O:HCl:HNO}_3$ (1:1:1) solution for 30 s. Microstructural characterization was carried out using an optical microscope and a field emission scanning electron microscope (NOVA NANOSEM 450). Vickers microhardness was measured using a microhardness testing machine (CSM International) at a load of 500 g with an indentation time of 10 s. A nano-hardness test was performed using nano-indentation equipment (TI 750, Hysitron Ltd.) equipped with a Berkovich indenter. The maximum indentation load of 8 mN was applied with $15\text{-}\mu\text{m}$ spacing between two consecutive indentations. The tensile tests were performed in a universal testing machine (INSTRON-1195) at room temperature with a crosshead speed of 1 mm/min.

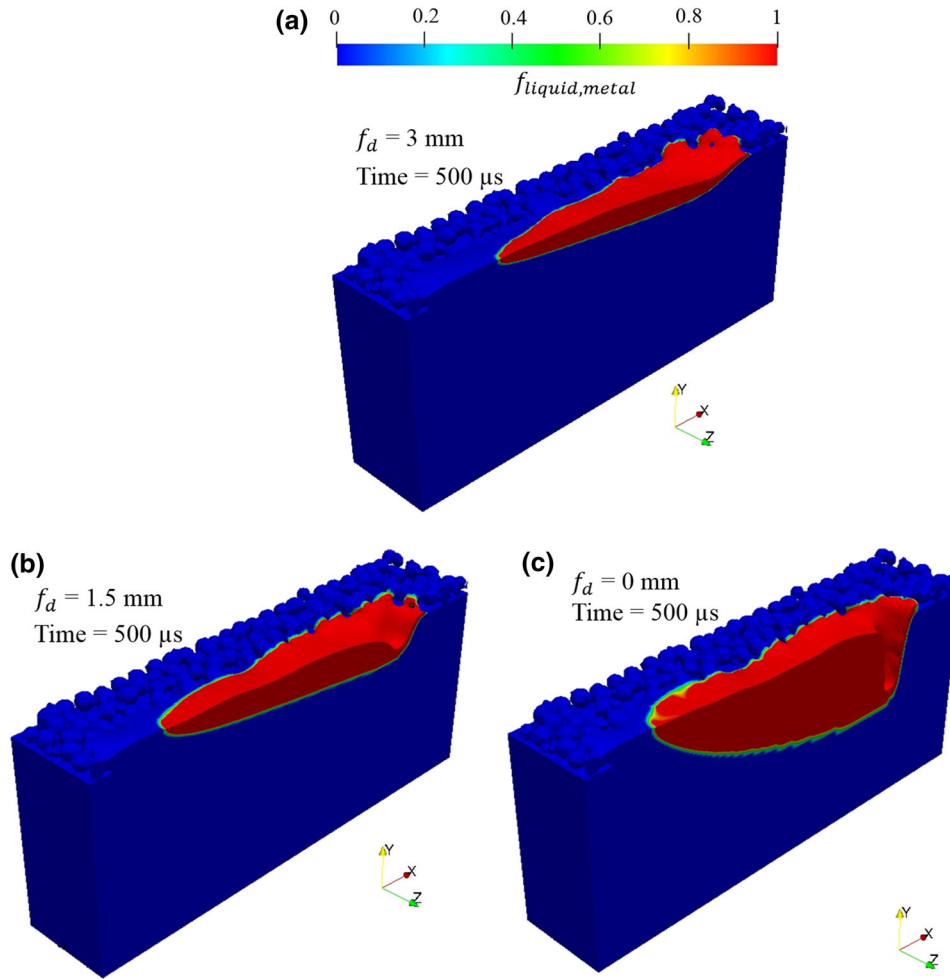


Fig. 2. Simulation results showing the effect of defocusing on melt pool morphology (longitudinal cross-sectional view). (a) Conduction mode, (b) transition mode and (c) keyhole mode.

RESULTS AND DISCUSSION

Computational Results of Single-Track Deposition

Single track scanning over a powder layer was simulated for three different defocus distances ($f_d = 0$ mm, $f_d = 1.5$ mm and $f_d = 3$ mm) keeping the power ($P = 100$ W) and velocity ($v = 0.7$ m/s) the same. The simulations were performed for 500 μ s in which a beam traverses a distance of 350 μ m. Figure 2 shows the longitudinal cross-section liquid fraction map at 500 μ s; the influence of defocusing on the melt pool morphology can be clearly seen. At $f_d = 3$ mm (Fig. 2a), the energy density is minimum ($E_d = 59.65$ J mm $^{-3}$); therefore, the maximum temperature is well below the boiling temperature of 316 L stainless steel; hence, the conduction mode prevails. The conduction mode is identified by a shallow and wide melt pool. However, as the laser beam is focused, i.e., decreasing the defocus distance, the energy density

increases, causing transformation of the melting mode from conduction to transition (Fig. 2b) and then from transition to keyhole (Fig. 2c). For the transition (Fig. 2b) and keyhole mode (Fig. 2c) of melting, melt pool depression below the beam can be clearly seen. This is due to recoil pressure, which starts dominating once the interface temperature exceeds the evaporation temperature. The recoil pressure exerts a downward force resulting in a topologically depressed cavity.

Figure 3 shows the transient evolution of the melt pool for $f_d = 0$ mm. In the figure the substrate, the unmelted powder layer and a deeply penetrated melt pool caused by recoil pressure can be clearly seen. As shown in Fig. 3, initially at 25 μ s, a small melt pool forms as laser irradiation starts. As the temperature exceeds the boiling point, the recoil pressure starts to act, and, due to melt displacement from the center of the melt pool, a bulge is formed. As the laser beam moves forward, the melt pool size increases and finally reaches a quasi-steady state. It

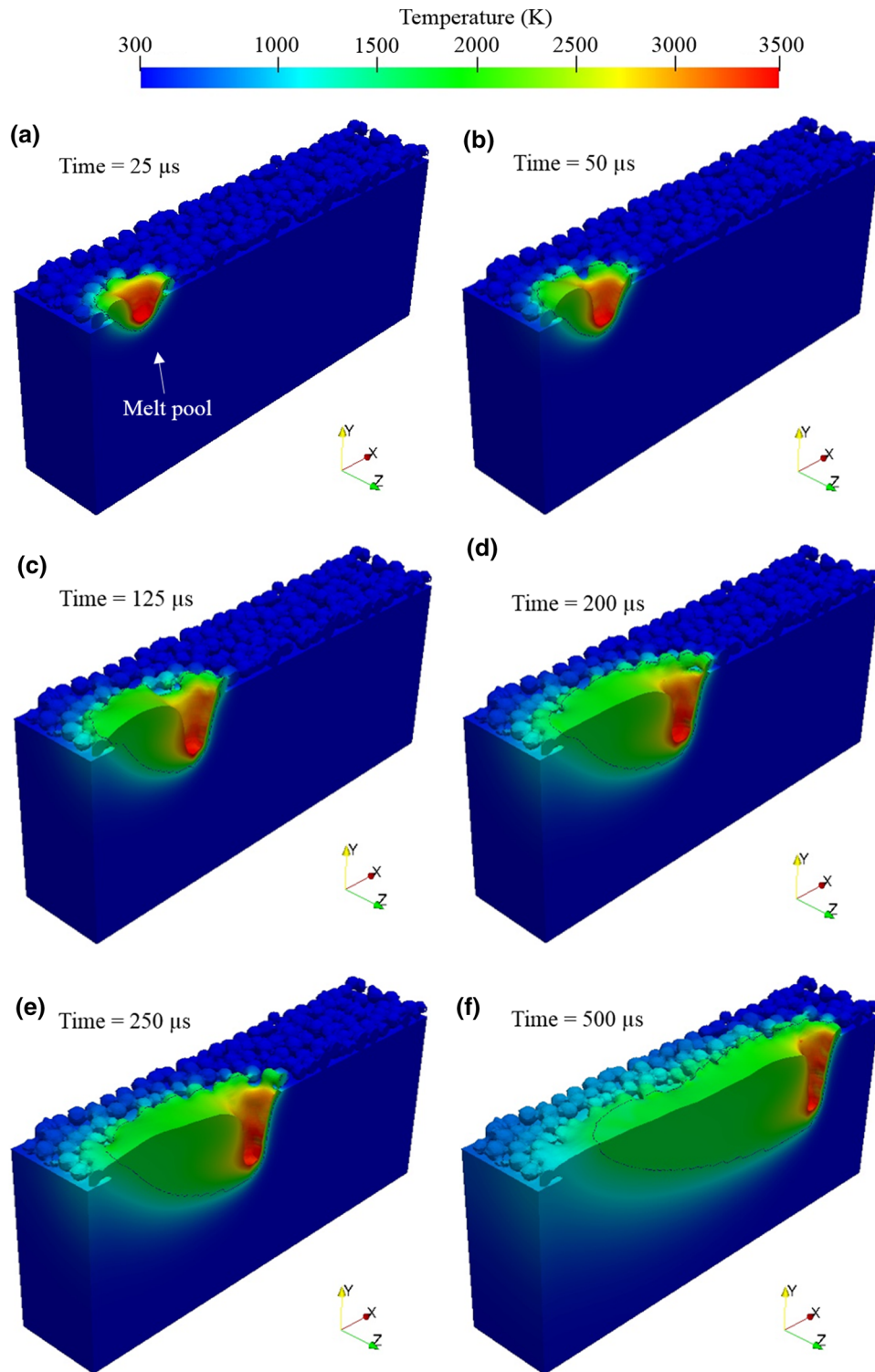


Fig. 3. Simulation results showing the melt pool formation during a deep penetration SLM (keyhole mode: $f_d = 0$ mm, $D_{spot} = 50 \mu\text{m}$, $E_d = 114.28 \text{ J mm}^{-3}$). (a) $t = 25 \mu\text{s}$, (b) $t = 50 \mu\text{s}$, (c) $t = 125 \mu\text{s}$, (d) $t = 200 \mu\text{s}$, (e) $t = 250 \mu\text{s}$ and (f) $t = 500 \mu\text{s}$.

can be seen that substantial melting of the substrate has taken place. The melting in the substrate is crucial in determining the surface morphology and metallurgical bonding of the solidified powder layer with the substrate.

Figure 4 shows maps of the temperature field along a cross section of the computational domain for the defocus distance of 3 mm and 0 mm, illustrating the melt pool evolution (melting and solidification) at different times. For $f_d = 3$ mm,

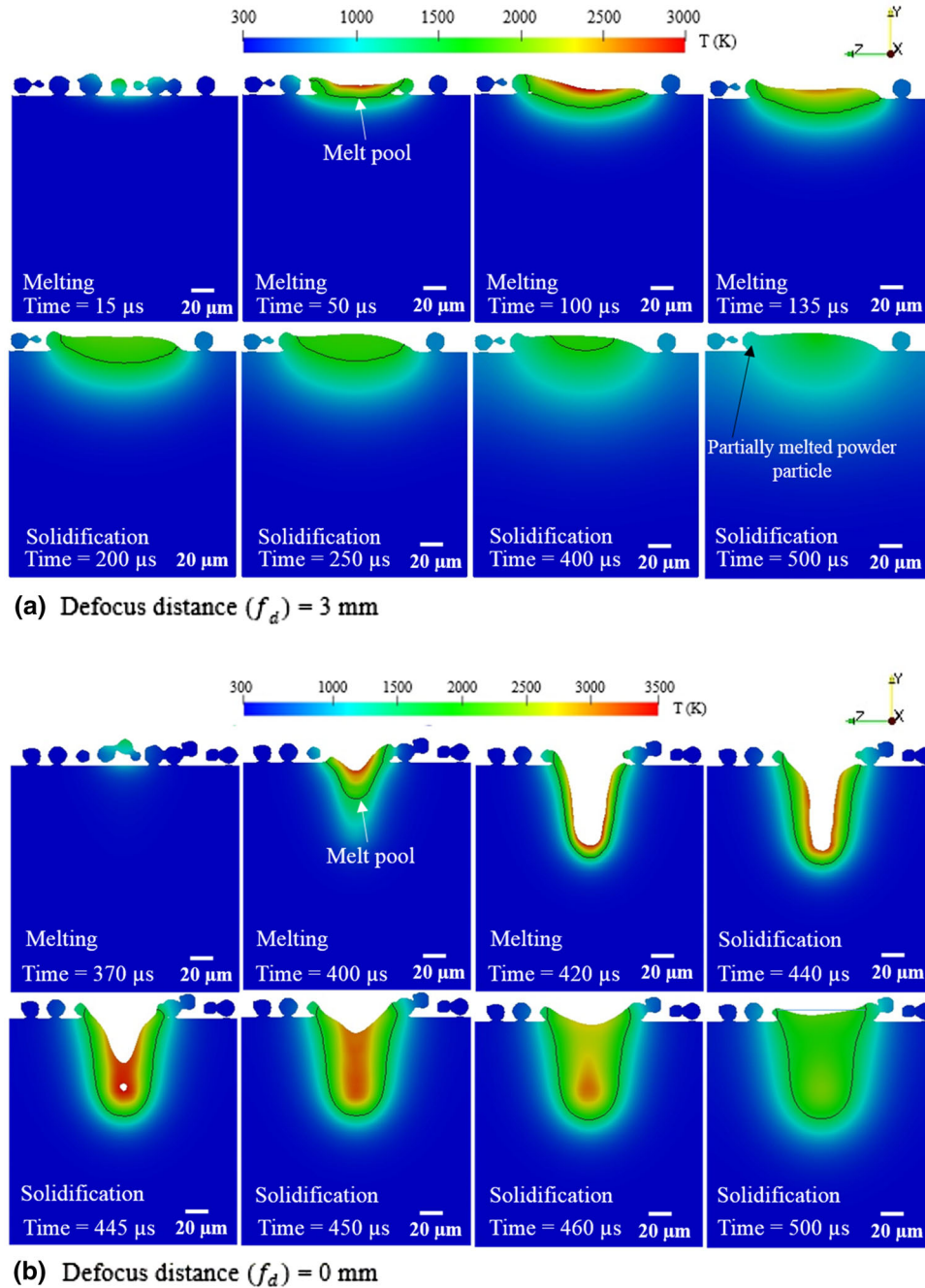


Fig. 4. Temperature field along a cross section of the computational domain showing the melt pool evolution. (a) Conduction mode and (b) keyhole mode.

monitoring plane $Y-Z$ is at a distance of $100\ \mu\text{m}$ along the X direction (Fig. 1), whereas for $f_d = 0\ \text{mm}$, monitoring plane $Y-Z$ is at a distance of $340\ \mu\text{m}$ along the X direction. Figure 4a shows the temperature field along the cross section for $f_d = 3\ \text{mm}$. As the laser beam approaches the monitored plane, the melt pool size and temperature increase steadily ($50\ \mu\text{s}$ and $100\ \mu\text{s}$) and reach the maximum when the laser beam is at the monitored plane ($135\ \mu\text{s}$). After $135\ \mu\text{s}$, as the laser beam moves away from the plane, the temperature drops,

and solidification starts. Complete solidification is achieved at $500\ \mu\text{s}$. As mentioned in the previous section, the $f_d = 3\ \text{mm}$ leads to the minimum energy density; therefore, the conduction mode of melting prevails. Figure 4a shows that an asymmetrical melt pool is formed because of the partially melted particle that remains stuck to the solidified molten pool. Figure 4b shows the temperature field along the monitored cross section for $f_d = 0\ \text{mm}$. At $400\ \mu\text{s}$, as the Gaussian beam approaches the monitored plane, the powder particles as well as

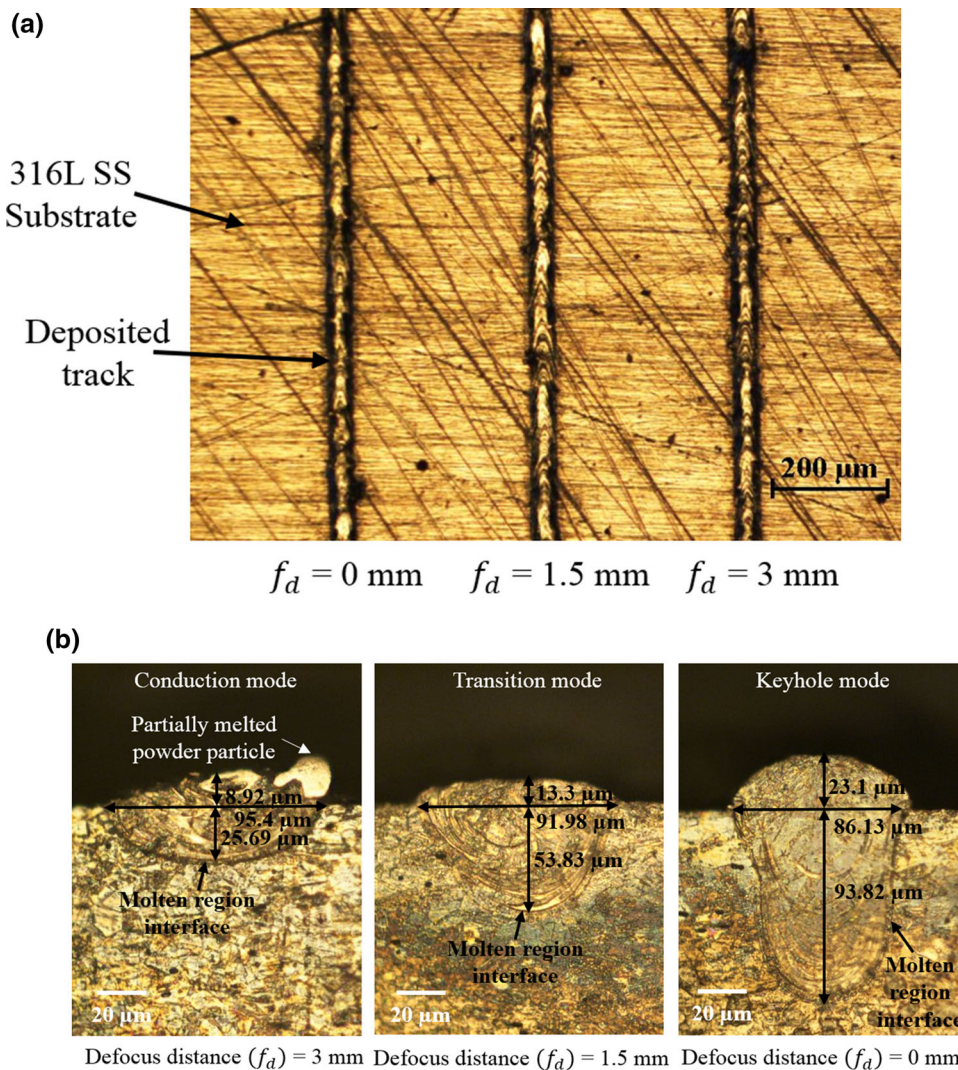


Fig. 5. Optical micrograph of the deposited single tracks after loose powder is removed from the substrate plate. (a) Top view and (b) cross-sectional view.

the substrate melt and merge into a melt pool. As the temperature exceeds the boiling point, the melt pool region directly underneath the laser beam is topologically depressed because of the recoil pressure. Since the recoil pressure depends exponentially on temperature (Eq. 18), its extent increases with rising temperature. At 420 μ s, the laser beam reaches the monitoring plane, and it can be seen that a narrow and deeper melt pool with a significantly depressed surface is formed. After 420 μ s, the laser moves away from the monitored plane, and molten metal starts filling the depressed region. The filling of molten metal causes recovery of the topologically depressed region. If the depressed region is substantially deep, then it may collapse with gas entrapped within it. As shown in Fig. 4b at 445 μ s, even though gas is trapped within the melt pool, it is ejected out (450 μ s) leading to porosity-

free single-track deposition. However, if the energy density is further increased, then recovery of the collapsed deep keyhole will not be achieved, leading to formation of spherical porosity. The collapse of the cavity can leave voids in the propagation path of the laser beam. Therefore, a deep keyhole is not preferable, as it will lead to porosity.

Experimental Validation and Observations

Figure 5a shows the top view of the deposited single tracks at three different defocus distances. Figure 5b shows the cross sections of the deposited single tracks. Clearly, the morphology of the molten pool experiences a transition from conduction to keyhole mode with decreasing defocus distance when the laser power, scanning velocity and layer thickness are fixed. For the samples deposited at $f_d = 3$ mm, the molten pool consists of a wider and

Table I. Quantitative comparison of melt pool dimensions for the single-track laser traversal obtained from experiments and the present model

f_d (mm)	Width (Expt), W_{Expt} (μm)	Width (Num), W_{Num} (μm)	$\frac{W_{\text{Expt}} - W_{\text{Num}}}{W_{\text{Expt}}}$ (%), difference	Depth of penetration (Expt), D_{Expt} (μm)	Depth of penetration (Num), D_{Num} (μm)	$\frac{D_{\text{Expt}} - D_{\text{Num}}}{D_{\text{Expt}}}$ (%), difference
0	86.13	84.67	1.69	93.82	88.5	5.67
1.5	91.98	91.304	0.73	53.83	41.7	22.53
3	95.4	102.89	- 7.85	25.69	20.5	20.20

narrow region, which is the typical characteristic of the conduction mode. As the defocus distance is further decreased, the molten pool transforms into the keyhole mode. Also, as observed in the simulation (Fig. 4a), a partially melted particle is observed around the periphery of the molten pool (Fig. 5b). It is also evident from Figs. 4 and 5b that the shape of the melt pool predicted by the present model is similar to the experimental profile.

Table I shows the quantitative comparison of the melt pool width and depth predicted by the model with the experimental results. As shown, the simulated melt pool width has good agreement with the experimentally determined width. The simulated substrate melting depth is slightly lower than the experimentally determined depth. The possible reasons for the slight under-prediction of the substrate melting depth could be because of internal reflection of the laser beam within the powder layer, which was not considered. The other possible reason could be the consideration of the temperature-independent thermophysical properties of the 316 L stainless steel in simulations.

Figure 6a and b shows the optical and FE-SEM micrographs of the fabricated 316L stainless steel cuboidal bulk specimen for conduction and keyhole mode, respectively. The characteristic feature of the layer-by-layer formation due to the unidirectional scanning strategy is seen clearly in the optical micrographs of the cross section of the bulk specimen. The optical micrograph clearly shows that the $f_d = 3$ mm leads to the formation of a shallow and wide melt pool, whereas the $f_d = 0$ mm leads to the formation of a deeper and narrow melt pool. The optical micrographs show that the samples are free from porosity and solidified molten tracks form good metallurgical bonding between the adjacent tracks as well as between the layers. To understand the effect of defocusing on the microstructure, FE-SEM micrographs at high magnification are reported. As shown in Fig. 6a, b, at first, for both defocus distances there is planar interface growth (zones CR1 and KR2); then, cellular grains form (zones CR2 and KR1), which grow epitaxially along the

maximum heat flux direction, i.e., perpendicular to the melt pool interface. Also, it can be observed that the keyhole mode results in finer cellular grains compared with the conduction mode. As the melting mode is transformed from conduction to keyhole, the mean cellular spacing decreases from about $0.45 \mu\text{m}$ to $0.28 \mu\text{m}$. This refinement in cellular grains in the keyhole mode is due to significant remelting of the previously deposited layers. In the course of remelting as the surrounding material is bulk solid, the cooling rate is enhanced because of faster heat dissipation resulting in fine grains.

Table II lists the results of various mechanical characterizations, such as microhardness, nanohardness, yield tensile strength (YTS), ultimate tensile strength (UTS) and percentage elongation to failure. Vicker's microhardness measurements are performed by taking ten indentations on a cross section parallel to the build direction. The reported average microhardness values indicate that the hardness is the minimum for the conduction mode sample, and it increases as the melting mode transforms to the keyhole mode. Following the same trend of microhardness, the results of the nanohardness test also show that the keyhole mode leads to the maximum hardness. The average nanohardness values under conduction, transition and keyhole modes are 3.89 GPa, 4.58 GPa and 4.7 GPa, respectively. The higher micro- and nanohardness for the keyhole mode is due to the finer grains in this mode compared with the other modes. From Table II, the influence of the melting mode on the tensile behavior can be seen; there is no substantial difference between the YTS and UTS for different melting modes. However, it is evident that the melting mode has a prominent effect on elongation to failure. The keyhole mode shows the highest ductility with percentage elongation to failure of 78.01%. Also, all samples in general show exceptionally high ductility due to the unidirectional scanning strategy for each layer. This leads to the formation of typical cellular grains with orientation parallel to the direction of the load.

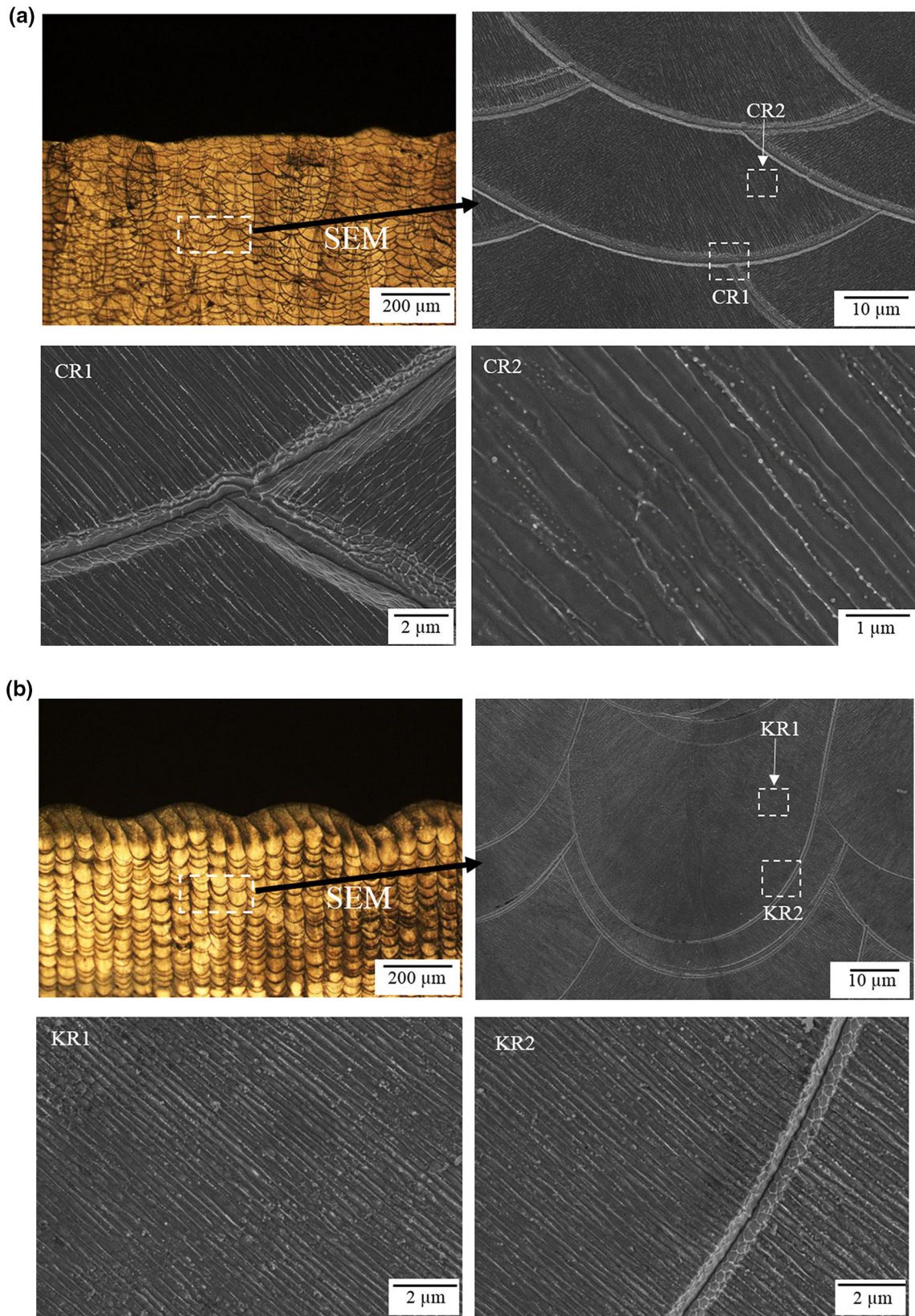


Fig. 6. Optical and FE-SEM micrographs displaying the melt pool boundaries and microstructure of the bulk specimen. (a) $f_d = 3$ mm; (b) $f_d = 0$ mm. CR: conduction region, KR: keyhole region.

Table II. Room temperature mechanical properties of various specimens prepared under different melting modes

f_d	Microhardness (HV1)	Nanohardness (GPa)	YTS (MPa)	UTS (MPa)	Elongation (%)
0 mm (keyhole)	213.67 ± 2.11	4.7 ± 0.15	465.46 ± 5.20	525.81 ± 6.44	78.01 ± 6.79
1.5 mm (transition)	211.16 ± 1.82	4.58 ± 0.18	461.14 ± 10.05	521.77 ± 6.70	70.45 ± 1.98
3 mm (conduction)	207.55 ± 2.73	3.89 ± 0.09	464.33 ± 5.13	524.68 ± 4.26	65.71 ± 8.12

CONCLUSION

This work reports a comparative study based on simulations and experiments for SLM of 316L stainless steel with different melting modes. The key finding can be summarized as:

1. It was found that the defocusing has a prominent effect on the SLM process. For focused laser beams, the keyhole mode of melting occurs where both the thermocapillary force and recoil pressure play a dominant role resulting in a narrow and deeper melt pool. On the other hand, for the defocused laser beam, the conduction mode of melting occurs where the thermocapillary force as the major driving force results in a wider and shallow melt pool.
2. Contrary to the common notion that keyhole mode results in inferior mechanical properties, it was found that if the mode of melting is stable keyhole, then porosity-free single-track deposition can be achieved having better mechanical and microstructural properties.
3. The microstructure in both the conduction and keyhole modes shows fine cellular grains. Compared with conduction mode, keyhole mode results in finer grains. As the melting mode transforms from conduction to keyhole mode, the mean cellular spacing decreases from about $0.45 \mu\text{m}$ to $0.28 \mu\text{m}$.
4. The mechanical testing results of the bulk specimen show that the stable keyhole mode results in substantially higher microhardness, nanohardness and elongation to failure compared with the conduction mode.

REFERENCES

1. W.J. Sames, F.A. List, S. Pannala, R.R. Dehoff, and S.S. Babu, *Int. Mater. Rev.* 61, 315 (2016).
2. W.E. King, H.D. Barth, V.M. Castillo, G.F. Gallegos, J.W. Gibbs, D.E. Hahn, C. Kamath, and A.M. Rubenchik, *J. Mater. Process. Technol.* 214, 2915 (2014).
3. Z. Saldi, A. Kidess, S. Kenjereš, C. Zhao, I. Richardson, and C. Kleijn, *Int. J. Heat Mass Transf.* 66, 879 (2013).
4. R. Fabbro, *J. Phys. D* 43, 445501 (2010).
5. M. Courtois, M. Carin, P.L. Masson, S. Gaied, and M. Balabane, *J. Phys. D* 46, 505305 (2013).
6. D.B. Hann, J. Iammi, and J. Folkes, *J. Phys. D* 44, 445401 (2011).
7. J.J.S. Dilip, S. Zhang, C. Teng, K. Zeng, C. Robinson, D. Pal, and B. Stucker, *Progr. Addit. Manuf.* 2, 157 (2017).
8. U.S. Bertoli, A.J. Wolfer, M.J. Matthews, J.-P.R. Delplanque, and J.M. Schoenung, *Mater. Des.* 113, 331 (2017).
9. J.L. Tan, C. Tang, and C.H. Wong, *Metall. Mater. Trans. A* 49, 3663 (2018).
10. T. Qi, H. Zhu, H. Zhang, J. Yin, L. Ke, and X. Zeng, *Mater. Des.* 135, 257 (2017).
11. G.E. Bean, D.B. Witkin, T.D. Mclouth, D.N. Patel, and R.J. Zaldivar, *Addit. Manuf.* 22, 207 (2018).
12. T.D. Mclouth, G.E. Bean, D.B. Witkin, S.D. Sitzman, P.M. Adams, D.N. Patel, W. Park, J.-M. Yang, and R.J. Zaldivar, *Mater. Des.* 149, 205 (2018).
13. J. Ciurana, L. Hernandez, and J. Delgado, *Int. J. Adv. Manuf. Technol.* 68, 1103 (2013).
14. K.-H. Leitz, C. Grohs, P. Singer, B. Tabernig, A. Plankensteiner, H. Kestler, and L. Sigl, *Int. J. Refract. Metals Hard Mater.* 72, 1 (2018).
15. C. Kloss, C. Goniva, A. Hager, S. Amberger, and S. Pirker, *Prog. Comput. Fluid Dyn.* 12, 140 (2012).
16. E.J. Parteli and T. Pöschel, *Powder Technol.* 288, 96 (2016).
17. C. Tang, J. Tan, and C. Wong, *Int. J. Heat Mass Transf.* 126, 957 (2018).
18. H.G. Weller, G. Tabor, H. Jasak, and C. Fureby, *Comput. Phys.* 12, 620 (1998).
19. N. Samkhaniani and M.R. Ansari, *Heat Mass Transf.* 53, 2885 (2017).
20. A.D. Brent, V.R. Voller, and K.J. Reid, *Numer. Heat Transf. B-Fund.* 13, 297 (1988).
21. S.A. Khairallah, A.T. Anderson, A. Rubenchik, and W.E. King, *Acta Mater.* 108, 36 (2016).
22. N. Pathak, A. Kumar, A. Yadav, and P. Dutta, *Appl. Therm. Eng.* 29, 3669 (2009).
23. T. Mukherjee, H. Wei, A. De, and T. Debroy, *Comput. Mater. Sci.* 150, 369 (2018).